Mode I and mode II fracture behavior in nano-engineered long fiber reinforced composites

Anh Tuan Le, Quentin Govignon, Samuel Rivallant, Thierry Cutard

To cite this version:

Anh Tuan Le, Quentin Govignon, Samuel Rivallant, Thierry Cutard. Mode I and mode II fracture behavior in nano-engineered long fiber reinforced composites. Polymer Composites, 2023, 44 (7), pp.4016-4026. 10.1002/pc.27374 . hal-04081911

HAL Id: hal-04081911
https://imt-mines-albi.hal.science/hal-04081911v1

Submitted on 28 Apr 2023

Mode I and mode II fracture behavior in nano-engineered long fiber reinforced composites

Anh Tuan Le[1,2] **Quentin Govignon**[1] **Samuel Rivallant**[2]
Thierry Cutard[1]

[1]Institut Clément Ader (ICA); Université de Toulouse; CNRS, IMT Mines Albi, INSA, ISAE-SUPAERO, UPS, Albi, France
[2]Institut Clément Ader (ICA); Université de Toulouse; CNRS, IMT Mines Albi, INSA, ISAE-SUPAERO, UPS, Toulouse, France

Correspondence
Anh Tuan Le, Institut Clément Ader (ICA); Université de Toulouse; CNRS, IMT Mines Albi, INSA, ISAE-SUPAERO, UPS, Campus Jarlard, Albi F-81013, France.
Email: leanhtuan@outlook.fr; anh_tuan.le@mines-albi.fr

Funding information
Bpifrance; Région Occitanie

Delamination still remains one of the common concerns in continuous fibers reinforced polymer composites. In the literature, the incorporation of nanoconstituents into constitutive composites plies has been suggested with the aim of improving interface toughness. In this study, vertically aligned carbon nanotubes forests (VACNTs) are transferred at composites interfaces, and mode I (DCB tests) and mode II (ENF tests) fracture tests carried out on composite samples. Microscopic analysis of reference and nano-engineered composites help to understand fracture behavior and toughness. While the crack path in ENF samples is observed at interlaminar VACNTs-resin interfaces, the crack path in DCB samples is intralaminar, located within the unidirectional carbon fiber plies. These microscopic observations give explanation for unstable crack propagation in nano-engineered ENF samples and the unchanged toughness from the nano-engineered to the reference zone in DCB samples.

1 INTRODUCTION

The incorporation of nanomaterials (carbon nanotubes (CNTs), graphene, nanoclay, nanosilica, and so forth) into composites to form nano-engineered composites has been investigated in the literature with the aim of improving their strength,[1,2] stiffness, [3] fracture toughness,[4] and fatigue properties.[5,6] Since the synthesis of CNTs in the 1990s,[7] this type of nanomaterial has been widely investigated due to its excellent mechanical properties, as well as its high thermal[8] and electrical conductivity.[9] In the literature, a noticeable enhancement in the thermal conductivity of resin-CNTs samples has been observed.[10–13] The addition of 1 wt% CNTs can increase the matrix's electrical conductivity by up to 10 orders of magnitude.[14,15]

Introducing dispersed CNTs is known to enhance not only the strength[16,17] and stiffness of composites[18,19] but also their fracture toughness.[20–22] However, the formation of local agglomerations of CNTs bundles during resin impregnation process is likely to create singularities and decrease the mechanical properties of the composites.[23,24] Functionalization and sonication steps help disperse CNTs into matrix, which can enhance the interface toughness in composite materials.[23,25–28] For example, Sun et al.[29] found that ozone-functionalization of CNTs improved dispersion and led to stronger interfacial bonding with the epoxy matrix. In the work of Gkikas et al.,[30] optimal sonication parameters (amplitude of dispersion and time) led to a 95% improvement in the interface toughness of nano-engineered composites with 0.5 wt% CNTs. Furthermore, the optimal mass ratio of

CNTs in the matrix has been reported in the works of Ayatollahi et al.,[31,32] where the ratio of 0.5–1 wt% CNTs was found to improve the bending behavior of nano-engineered composites the most.

Mixing CNTs with other constituents allows for a resonant reinforcement effect on interface behavior. Merging spherical particles into CNTs bundles increases 409% G_{Ic},[33] while blending silica and CNTs bundles can result in a 37% improvement in G_{Ic}.[34] In addition, a 24% fracture toughness enhancement is observed thanks to the synergy of CNTs and reactive oligomer.[35]

Veedu et al.[36] directly synthetized CNTs on woven SiC fibers, a strong CNTs-fibers bonding makes nano-engineered composites 348% tougher in mode I fracture and 54% tougher in mode II fracture than reference samples.

In the study by Wicks et al.,[37] short CNTs (6 μm in height) and long CNTs (20 μm in height) are directly synthetized on woven fibers. Aerospace epoxy-based composites are consolidated at vacuum pressure and marine epoxy-based composites are consolidated by hand molding. In the aerospace composites, the presence of long CNTs increases the G_{Ic} value by 32% compared with the reference composite, but this value decreases by half in short CNTs. In the case of marine epoxy-based composites, CNTs integrated in composites increase the mode I toughness value by at least 89% in both cases (short and long CNTs). The toughness may depend on the impregnation process and CNTs height.

Salas et al.[38] perform ultrafast growth of CNTs directly on recycled carbon fibers, which is then impregnated with resin and consolidated. The results of mode I fracture toughness show that the presence of CNTs decreases G_{Ic} value by 35% for nano-engineered composites with polypyrrole deposition and by 29% for nano-engineered composites with ferrocene deposition.

In this study, the initial vertically aligned carbon nanotubes (VACNTs) morphology is maintained vertically aligned after the impregnation process, which is inspired by these aforementioned works. In the study of Garcia et al.,[39] VACNTs are transferred onto unidirectional prepreg surface. The results from mode I fracture tests show that G_{Ic} toughness increases by 36% (for AS4/8552 composites) and 43% (for IM7/977-3 composites) with the presence of VACNTs at interfaces.

Ni et al.[40] use VACNTs that are 20 μm in height to transfer them onto unidirectional prepreg AS4/8552. Little difference in toughness is observed while comparing the reference and nano-engineered composites.

Falzon et al.[41] use unidirectional prepreg and VACNTs that are 80–100 μm in height to manufacture nano-engineered composites, VACNTs are transferred onto the prepreg surface by resin capillarity. For T700/SE84LV composites, with the presence of the VACNTs, the authors observe a 61% increase in G_{Ic}. For the T700/M21 composites, the G_{Ic} value increases by 31% in nano-engineered composites.

These aforementioned investigations demonstrate that the presence of nanoconstituents is beneficial for reinforcing both mode I and mode II toughness. However, local agglomeration of nanoconstituents and increased thickness due to the incorporation of nanoconstituents are likely to reduce the fracture toughness of the interface. The objective in this work is not only to compare the fracture behavior of reference composites (without VACNTs) with that of nano-engineered composites (with VACNTs in the interface), but the work is also completed by deducing the role of VACNTs in fracture toughness by observing the microstructure of postmortem composite specimens.

To achieve this objective, two main steps were followed. First, the determination of mode I and mode II toughness in M55J/M18 composites was carried out in both reference zones and nano-engineered zones. These experimental results allow to compare the fracture behavior of reference and nano-reinforced composites. After obtaining these quantitative or qualitative fracture toughness results, postmortem specimens were observed at the microscale with the objective of gaining in-depth insights of such toughness results shown at the macroscale. Conclusions were drawn regarding the concordance between microstructure in the nano-engineered zones and toughness behavior.

2 EXPERIMENT SECTION

2.1 Constituent materials

In this study, the first constituent used in the manufacturing process is Hexply® M18/32%/UD116/M55J/6K/300mm prepreg, which comprises M55J carbon fibers and M18 thermoset epoxy resin. One cured, M18 has a glass transition temperature of 198°C, and its viscosity at 60 and 80°C before curing is 300 and 80 Pa.s, respectively. The second constituent, VACNTs forest synthetized on aluminum-based wafer, reinforces the interface between two prepreg plies. The main properties of VACNTs synthetized by the industrial partner NAWATechnologies using Continuous chemical vapor deposition are: a density of approximately 5.10^{11} VACNTs/cm^2, a height of 20 ± 8 μm, and an average diameter of 8 nm. To facilitate the transfer of VACNTs onto the prepreg surface, unidirectional prepreg is privileged in this study to minimize the level of fibers' waviness.

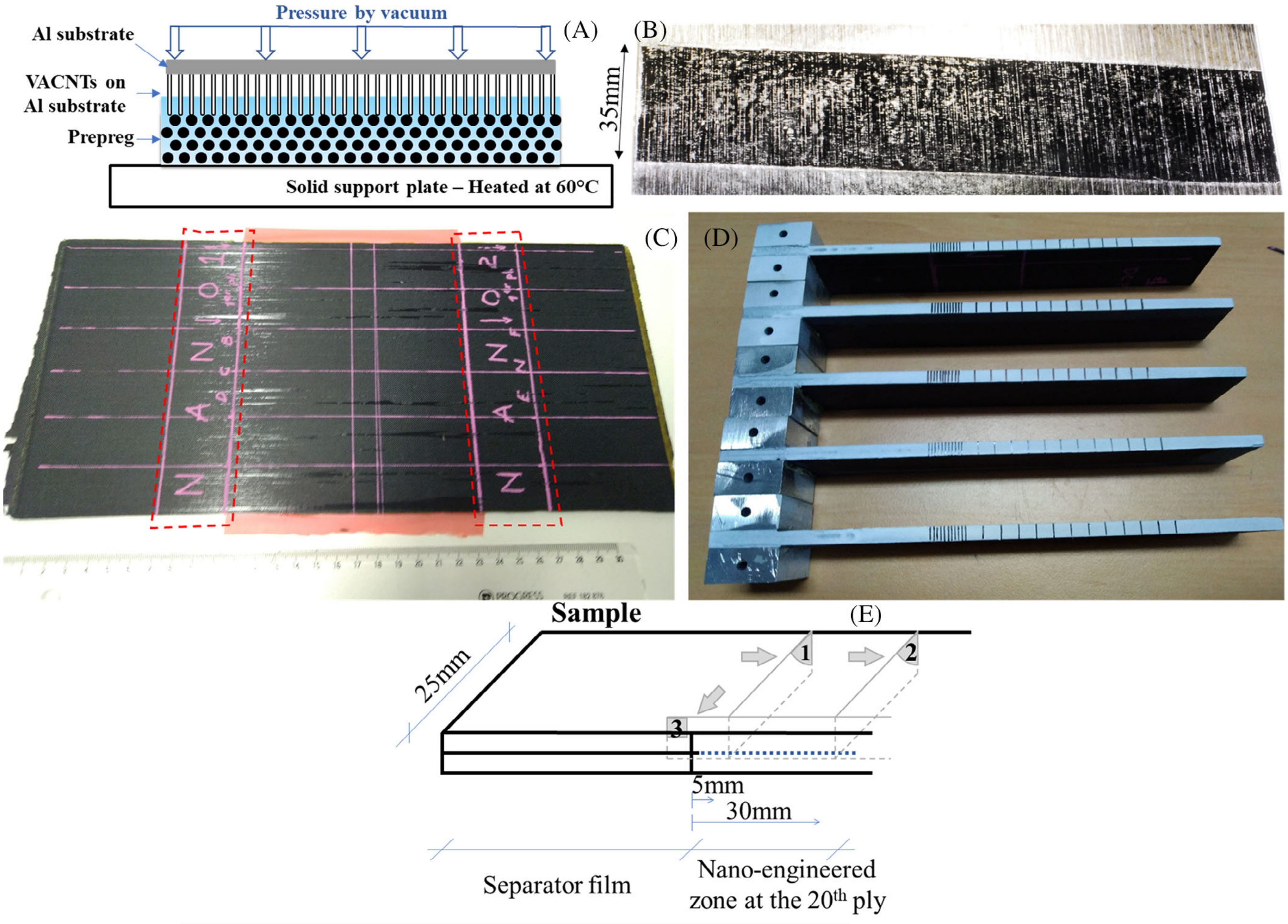

FIGURE 1 (A) VACNTs bonded to prepreg surface by vacuum; (B) VACNTs forests transferred onto the 20th prepreg ply; (C) Composite plate after the consolidation in autoclave; (D) Five DCB samples with loading blocks; (E) Positions of transversal cross-sections (n°1&2) and longitudinal cross-section (n°3) view for microscopic observations in $(0°)_{40}$ composite samples.

2.2 Preparation of nano-engineered composite materials

Initially, VACNTs synthetized on an Al-based substrate are bonded on top of a prepreg surface. The entire sample including prepreg, VACNTs and Al substrate is placed in a vacuum to uniformly distribute pressure at the VACNTs-prepreg surface, as illustrated in Figure 1A. The sample is heated to 60°C from the solid support plate using an oven. The viscosity of M18 resin at 60°C allows to control the capillary impregnation of the resin in the VACNTs forests. Following heating, the sample is then left to cool to 16°C, the high viscosity of M18 resin facilitates bonding between the VACNTs forests and the prepreg surface. The Al-based substrate is subsequently removed from the VACNTs forests. This nano-reinforced ply is situated between the 20th and the 21st plies in the $(0°)_{40}$ stacking sequence (see Figure 1B). A precrack is guided by a separator film at that same ply interface.

In autoclave, the consolidation at 180°C with 8 bar of pressure for 2 h allows to cure the M18 thermoset resin. Figure 1C illustrates the nano-reinforced composite plate after autoclave consolidation. This plate is then cut into small samples for ENF tests and DCB tests, and a red separator film was already inserted between the 20th and 21st plies to create a precrack, nano-engineered zones also lie in the middle of 20th and 21st plies within the red dotted frames. The nano-reinforced composite samples intended for DCB tests are shown in Figure 1D, with the edges painted to facilitate tracking of crack propagation via a camera during DCB testing.

After mechanical testing, *postmortem* samples are embedded in potting resin to preserve the samples, including the delamination-induced crack path. Following consolidation of the potting resin at ambient temperature, the *postmortem* samples are cut into cross-sections, both from 5 to 30 mm from the end of the separator film, as well as into longitudinal sections, as depicted in

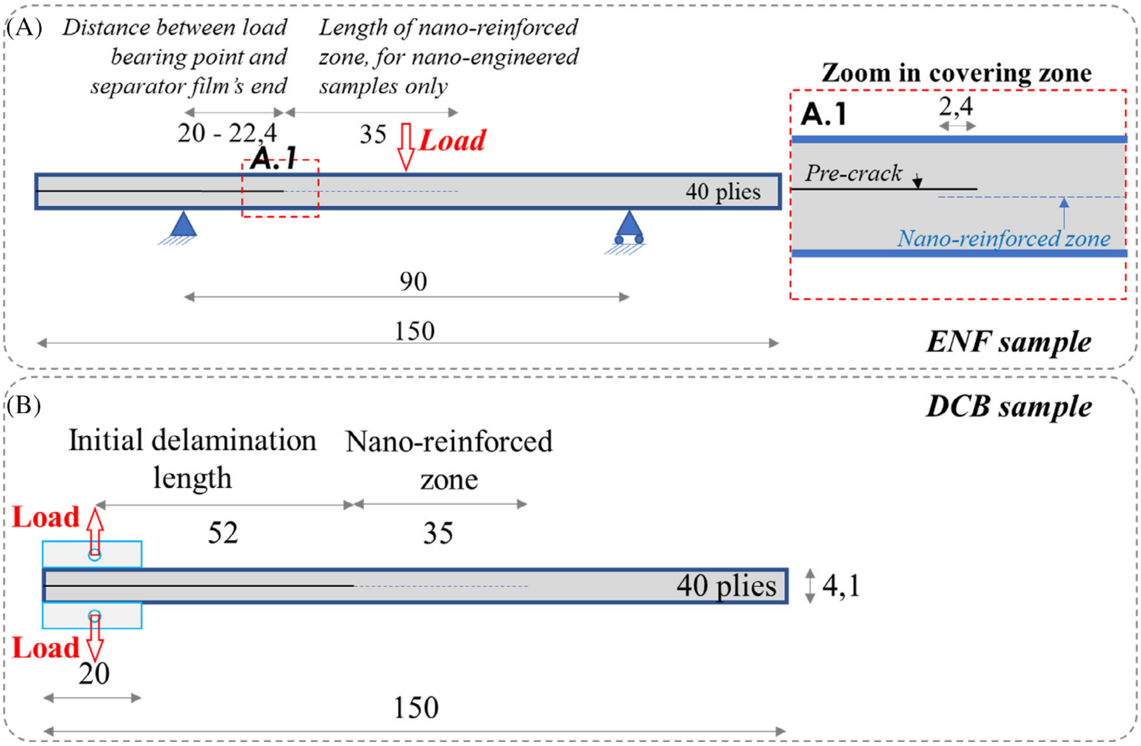

FIGURE 2 (A) Reference and nano-engineered ENF sample dimensions (mm); (B) DCB sample dimensions (mm), nano-reinforced zone covers 35 mm.

Figure 1E. The cut surfaces are subsequently polished for microscopic observations.

2.3 Testing methods

2.3.1 End notched flexure tests

Figure 2A shows the dimensions of one ENF sample amongst five reference samples and four nano-engineered samples. It is noted that both the reference ENF samples and the nano-engineered ones have the same dimensions. Their total length and width values are 150 and 25 mm, respectively, with a thickness of 4 mm corresponds to $(0)_{40}$ stacking sequence. For the nano-engineered samples, the VACNTs layer reinforces the resin between the 20th and the 21st plies. There exists a covering zone where separator film's end covers the beginning of the VACNTs layer, as shown in Figure 2A.1, this transition zone can guide the initial cracking path in nano-reinforced zone.

The suggested dimensions and installation followed the ASTM D7905 standard.[42] The tests were performed in displacement control mode with a constant displacement rate of 1 mm/min. Due to the unstable crack propagation at the very first loading in the case of nano-engineered samples, the mode II interlaminar fracture toughness G_{IIc} cannot be reported. However, the initial G_{IIc} can be computed by the simple beam theory at (Equation 1) from the work of Davies et al.[43]

$$G_{\mathrm{IIc}} = \frac{9P^2a^2}{4b^2E_1h^3}. \tag{1}$$

With P the force applied to center loading roller, a the delamination length ($a = a_0 = 20\,\mathrm{mm}$ because the initial delamination length can be considered as the pre-crack length), $b = 25\,\mathrm{mm}$ the specimen width, E_{1f} the flexural modulus of the specimen (determined from (Equation 3) from DCB testing), $h = 2\,\mathrm{mm}$ the specimen half-thickness.

2.3.2 Double cantilever beam tests

DCB samples preparation and testing followed the ASTM D5528 standard.[44] The samples were manufactured from the same plate as the ENF samples. Figure 2B shows the dimensions of one DCB sample amongst five nano-engineered samples. DCB samples share some identical dimensions with ENF ones: each sample's total length and width values are 150 and 25 mm, respectively, with a thickness of 4 mm corresponding to $(0)_{40}$ stacking sequence, the VACNTs interply was placed between the

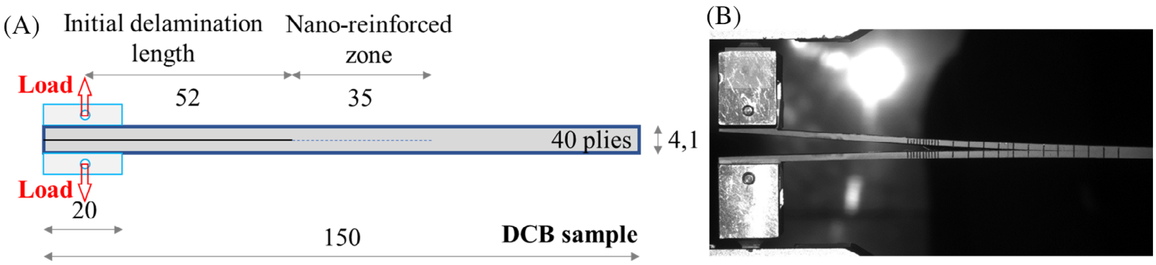

FIGURE 3 (A) DCB sample dimensions (mm): Nano-reinforced zone covers 35 mm; (B) DCB sample during the test.

20th and the 21st plies. The separator film inserted into 20th–21st plies creates a precrack, and the transition zone (where the separator film covers the beginning of the VACNT forests) helps guide the initial crack path in the nano-reinforced zone. Given that the nano-engineered zone covers only the first 35 mm, the zone beyond 35 mm can be considered as a reference zone. The tests were performed in displacement control mode with a constant displacement rate of 1 mm/min.

The quantitative comparison of mode I toughness in the nano-engineered zone and in the reference zone can be assessed by determining G_{Ic}:

$$G_{\mathrm{Ic}} = \frac{3P\delta}{2b(a+|\Delta|)}, \tag{2}$$

where G_{Ic} represents mode I interlaminar fracture toughness, P the load, δ the load point displacement, b the sample width, a the crack length. In addition, Δ is the correction value for beam root rotation and transverse shear of the arms. According to the standard, Δ is determined by establishing the regression curve of the compliance as a function of the cube of the delamination length (Figure 3).

Furthermore, the flexural modulus of the specimen can be determined using the following equation, as per the standard:

$$E_{1f} = \frac{64\,(a+|\Delta|)^3 P}{\delta b h^3}. \tag{3}$$

With a the crack length, Δ the correction value, P the load, δ the load point displacement, b the sample width, h the specimen half-thickness.

The purpose of this study is to investigate the correlation between microscopic analysis and mechanical behavior at nano-reinforced interfaces. To achieve this, the paper begins with the results of microscopic observations to scrutinize the crack propagation path after performing the fracture toughness tests. This allows us to deduce whether these results are consistent with the macroscopic mechanical response.

3 RESULTS AND DISCUSSION

3.1 End notched flexure tests

3.1.1 Microscopic observations

After having embedded the samples in potting resin, they were cut into cross-sectional and longitudinal sections, and the surface was then polished for microscopic observations. Figure 1E illustrates the positions of the transverse cross-sections (n°1&2) and longitudinal cross-section (n°3), which will be further described in the following figures.

Figure 4A shows a global optical microscopy image of the longitudinal cross-section (n°3) after crack propagation in the nano-reinforced zone. In the same section, a zoomed-in image in zone B, including the separator film's end, allows to observe the crack initiation, while zones C&D show the crack propagation path. These images demonstrate that the crack initiation and propagation occur exclusively at the VACNTs-resin interface throughout the nano-engineered zone.

Figure 5 shows the transverse cross-sectional n°1 view of the same nano-engineered ENF specimen. These images also confirm that the crack does not propagate within the fibers-resin intraply, but instead propagates at the VACNTs-resin interface. Only few fibers remain on the crack side of the VACNTs forests.

During the mode II toughness test, shearing stress between the through-thickness inferior beam and the superior beam deforms the resin between the 20th and 21st ply, resulting in the formation of cusps.[45] Figure 6 displays top views of fracture surfaces in reference ENF sample and nano-engineered ENF sample, respectively, with observations focused close to the crack initiation zones. In both samples, resin cusps can be observed and can be attributed to the high local strain levels of the resin. The reference ENF sample displays a higher cusps area density than the nano-engineered ENF sample, with larger cusps on average. These differences can be attributed to the difference in size of the resin volumes in the two composite types after consolidation. In the

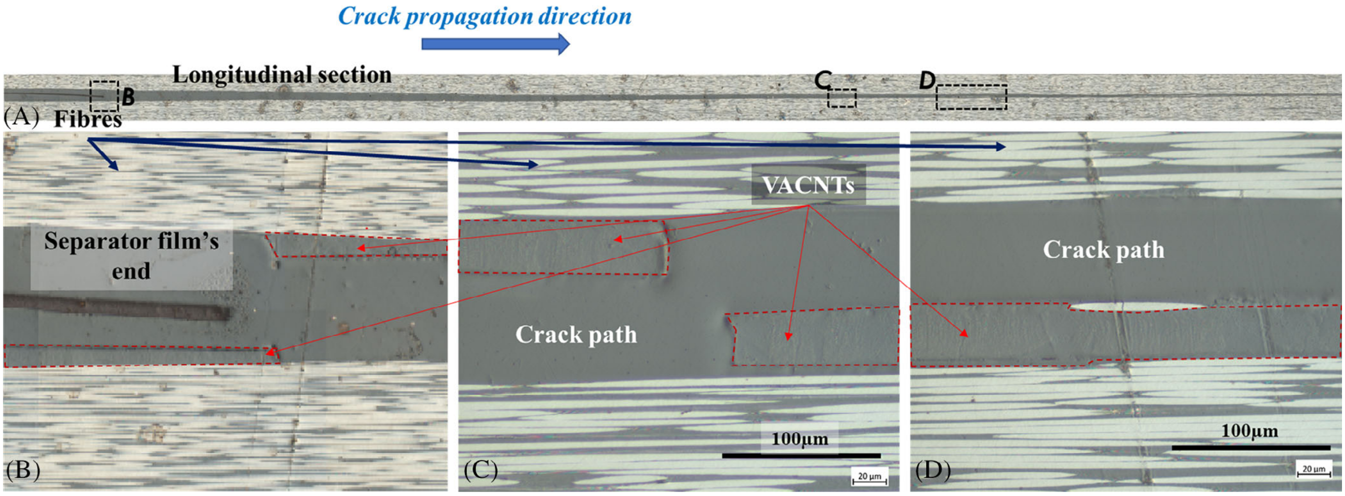

FIGURE 4 (A) Global view of crack path observed by optical microscopy in an ENF sample (longitudinal cross-section); (B) Crack initiation at the VACNTs-resin interface guided by separator film's end; (C and D) Crack propagation path at the VACNTs-resin interface.

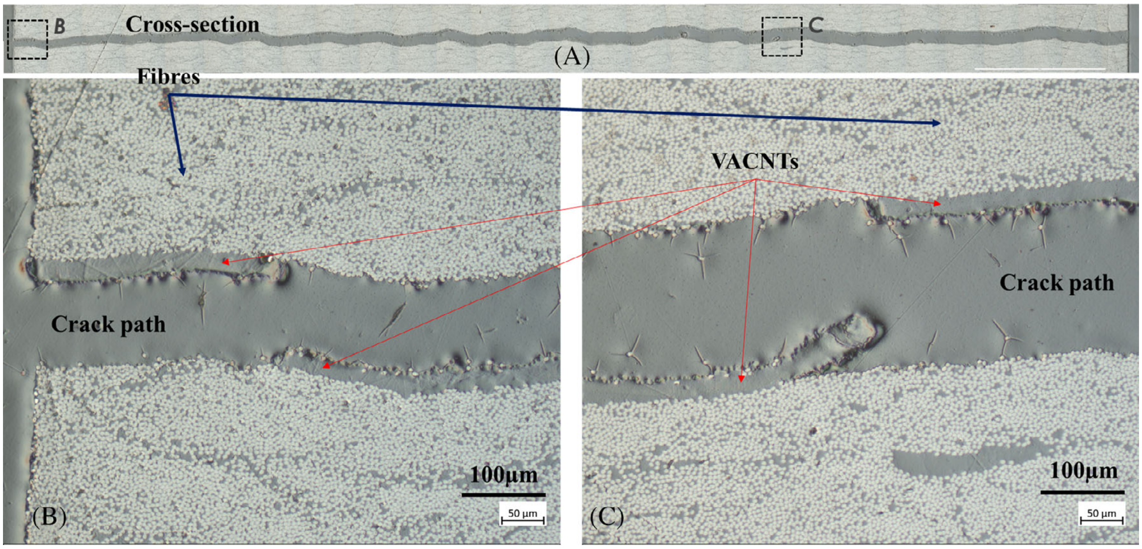

FIGURE 5 (A) Optical images of transverse cross-section (n°1) of the ENF sample at the nano-engineered interface: Crack propagation at the VACNTs-resin interface; (B) and (C) depict two magnified regions of (A).

nano-engineered composites, due to the presence of VACNTs, the volumes of deformable resin at the fracture interface are smaller. In the case of the reference composite, the volumes of deformable resin are higher. It can be considered that the presence of VACNTs at the interply decreases the volume of deformable resin at the fracture interface. The size of the cusps and their density therefore decrease at the observed interface.

3.1.2 Mechanical behavior

Figure 7 shows the load–displacement curves during ENF tests of four nano-engineered specimens and one representative reference specimen. Additional load–displacement profiles for the reference specimens in ENF tests are presented in Figure S1.

In Figure 7, the average value of the first loading until crack initiation in reference samples (2100 N) is 70% higher than that in nano-engineered samples (1238 ± 133 N). Figure S2 illustrates crack propagation which instantaneously propagated over a span of 2.8 cm in the nano-engineered sample at the very first loading, while Figure S3 shows the crack propagation in the reference sample at the end of the third loading. Furthermore, the average value of the first loading until crack in reference samples (2039 N) is 65% higher than the one in nano-engineered samples (1238 N). The comparison of

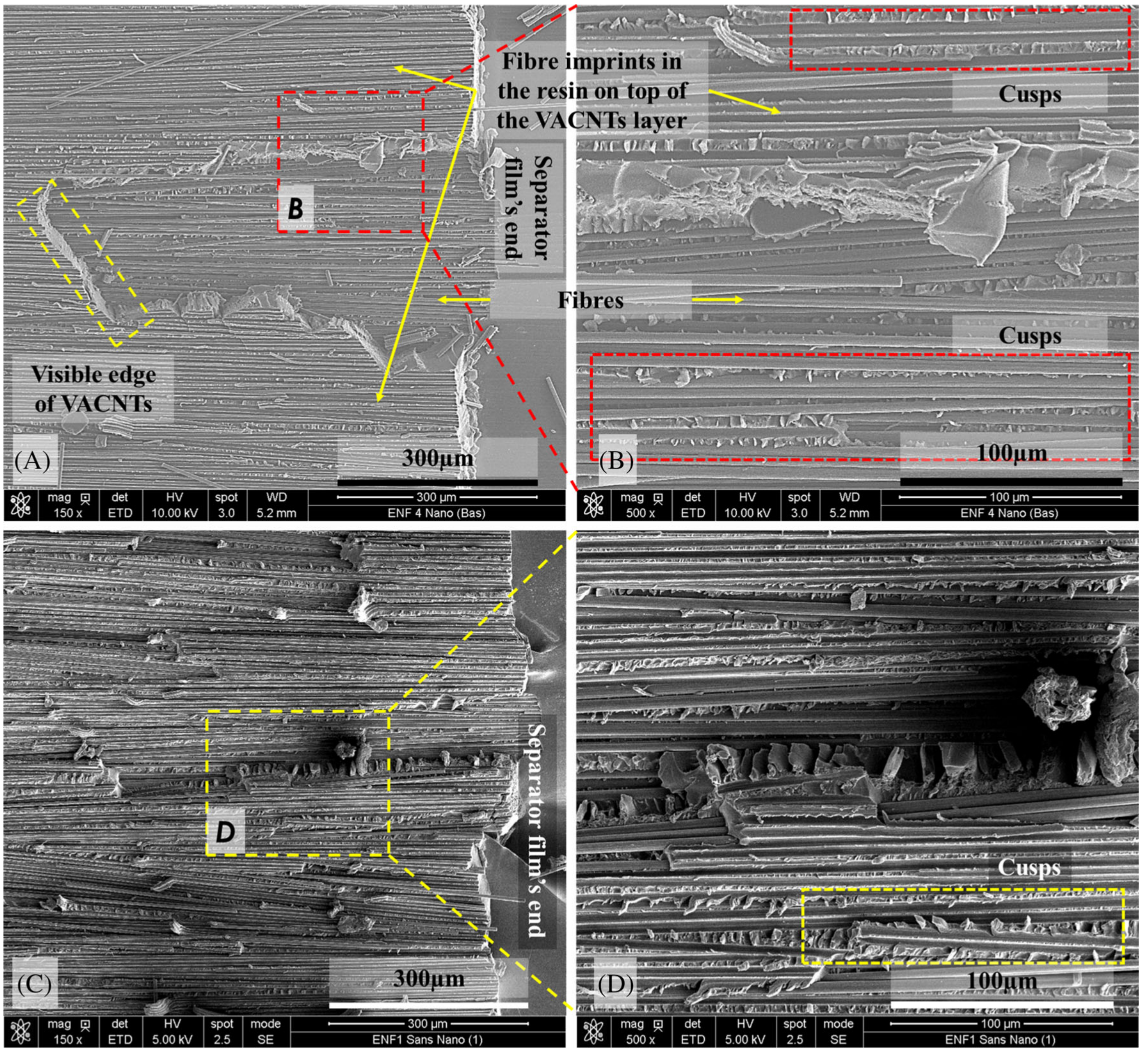

FIGURE 6 SEM images—(A and B) Top view of nano-engineered ENF fracture surface: crack path located at VACNTs-resin interface, fibers imprinted in the resin are observed on top of the VACNTs layer, observation of small resin cusps with low density occurs *postmortem*; (C and D) Top view of reference ENF fracture surface, observation of large resin cusps with high density.

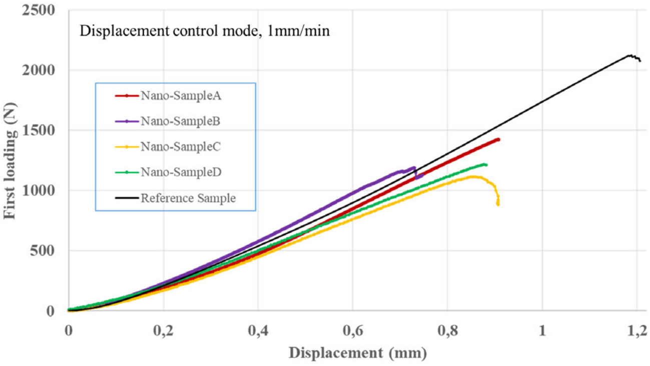

FIGURE 7 Load–displacement curves in the first loading of four nano-engineered samples and one representative reference sample.

these figures and values indicates that the presence of VACNTs forests can cause crack propagation instability at an earlier stage in mode II.

Table 1 summarizes the G_{IIc} values at crack initiation in both reference and nano-engineered composites. The value of G_{IIc} is calculated using (Equation 1), with $P_{\max}$ being the value of the load at crack initiation, $a = a_0 = 20$ mm the initial precrack length, $b = 25$ mm the specimen width, $E_{1f} = 330$ GPa the flexural modulus of the specimen, and $h = 2$ mm the specimen half-thickness. The results show that the presence of VACNTs in the interlaminar plies decreases the G_{IIc} values by 62%, from 567 to 211 N/m^2.

From a mechanical behavior standpoint, the presence of VACNTs at the interface does not improve mode II toughness in the studied nano-engineered composites.

The mechanical test results are consistent with the previous microscopic observations, which show that the size and the density of cusps in the nano-engineered interface decrease as a result of the reduction in deformable resin volume due to the presence of VACNTs.

TABLE 1 G_{IIc} in reference ENF composites and nano-engineered ENF composites.

		ENF-1	ENF-2	ENF-3	ENF-4	ENF-5	Average
Reference	P_{max} (N)	1991	2125	1997	2071	2010	2039
	G_{IIc} (N/m^2)	540	616	544	585	551	567
Nano	P_{max} (N)	1427	1191	(–)	1117	1217	1238
	G_{IIc} (N/m^2)	278	193	(–)	170	202	211

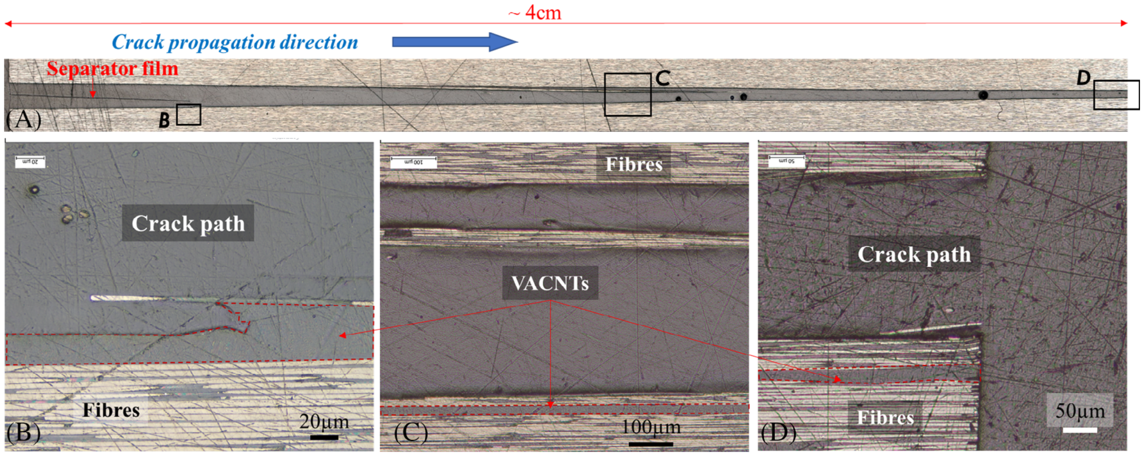

FIGURE 8 Longitudinal cross-section of a DCB sample in the nano-reinforced zone. The crack path initiates and propagates at an intralaminar interface throughout the observed area, and not at the VACNTs-resin interface.

These elements make the nano-engineered interface more unstable for crack propagation.

Microscopic and macroscopic results from the mode II ENF tests provide insights into the role of VACNTs at the interface of composites. Having known this tendency, DCB tests were also investigated for better understanding of the effect of introducing VACNTs in mode I toughness reinforcement.

3.2 Double cantilever beam tests

3.2.1 Microscopic observations

Sample cutting and preparation for DCB transverse and longitudinal cross sections was performed using the same method as for the ENF samples in Figure 1.

Figure 8A shows the global longitudinal cross-section of the crack propagation path in the nano-engineered zone. Stand-alone fiber located in the zoomed image B supports the previous analysis that the crack path propagates at fibers-resin interface. As demonstrated in images C&D, the further the crack continues to propagate, the higher the number of fibers pulled from the top ply to remain on the VACNTs interface side. The crack propagates at the fibers-resin intralaminar interface instead of the VACNTs-resin interface. The transverse cross-section view at 5 and 30 mm from the precrack zone in Figures 9 and 10 also asserts the intraply crack propagation path, but it is observed that the crack has propagated alternatively within the top and bottom ply around the nano-engineered interface. It is also to note that the crack can occur at the VACNTs-resin interface in some local zones at 5 mm from the crack initiation point, as shown in Figure 9B,D, but these zones are not representative and disappear at 30 mm from crack initiation point.

Furthermore, Figure 11 gives the top view of a fracture surface close to the crack initiation zone, revealing the transition between the end of the precrack zone and the beginning of the crack initiation path. Thus, the crack initiation occurs at adjacent fibers-resin interface instead of VACNTs-resin interface. Figure 11B shows the coexistence of fibers zone and fiber-imprinted zones, which provides additional information on the crack initiation mechanism. In conjunction with the preceding figures, it can be deduced that the fiber-resin crack path is observed from the initial stages to the crack propagation zone.

3.2.2 Mechanical behavior

Figure 12 presents the evolution of G_{Ic} as a function of the crack length a. It should be noted that the nano-engineered zone covers the first 35 mm of the crack

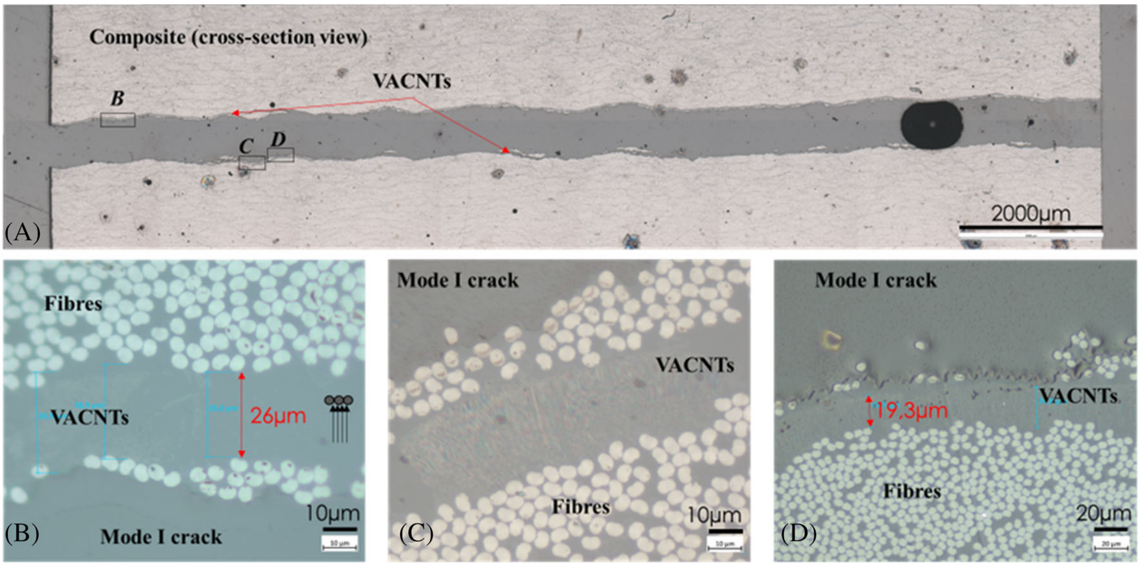

FIGURE 9 (A) Transverse cross-section of a DCB sample in the nano-engineered zone, at 5 mm from the crack initiation point. The crack propagation occurs at an intralaminar interface. (B), (C) and (D) depict three magnified regions of (A).

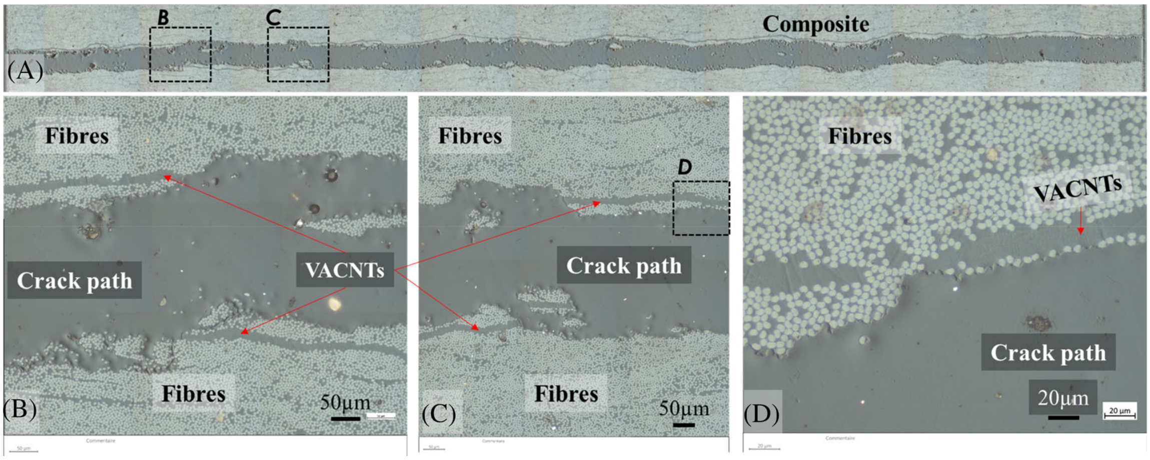

FIGURE 10 Transverse cross-section of a DCB sample in the nano-engineered zone, at 30 mm from the crack initiation point. The crack propagation occurs at an intralaminar interface.

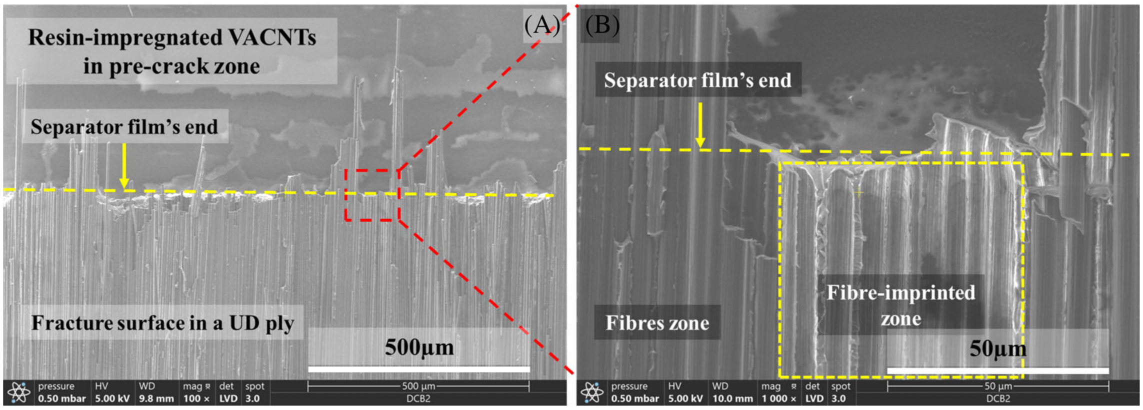

FIGURE 11 SEM images—Top view of the fracture surface of a nano-engineered DCB specimen, with a focus on the crack initiation zone. The crack initiation and propagation are observed in adjacent composite ply, rather than the VACNTs-resin interface. (B) depicts a magnified region of (A).

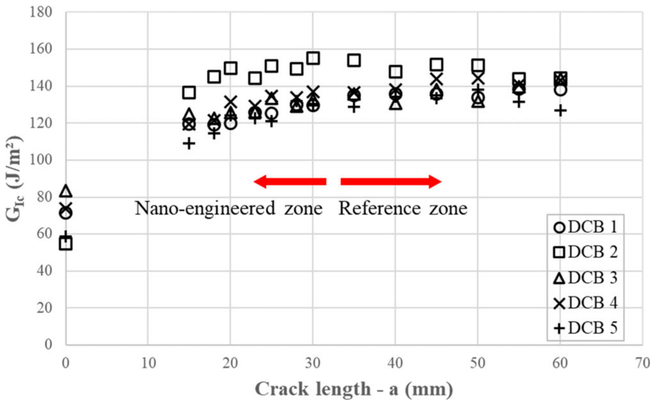

FIGURE 12 DCB tests—Mode I fracture toughness as a function crack length. VACNTs at the interface cover the first 35 mm of crack path. The zone further than 35 mm are reserved for reference zone.

propagation, and the reference zone covers the remaining length. At nano-engineered interface, from 20 to 30 mm of crack length, G_{Ic} values are stable, with an average value of 133 J/m^2. At reference interface, from 35 to 50 mm of crack length, G_{Ic} values remain stable with a value of 139 J/m^2. There is no significant difference between G_{Ic} in the nano-engineered zone and the reference zone. In the studied case, it can be considered that the presence of VACNTs does not significantly modify the mode I toughness. Figure S4 displays the load–displacement curve of the fifth DCB sample, which demonstrated similar behavior to the other DCB samples.

This DCB mechanical test results are in agreement with microscopic observations. It is observed on microscopic scale that the crack path initiates and continues to propagate in intralaminar zone in the vicinity of impregnated VACNTs. The more the crack propagates, the more the crack path moves away from nano-engineered interface and always stays in upper or lower side, as shown in Figure 8B–D. Interlaminar G_{Ic} value shows little difference in nano-engineered zone and reference zone because resin in intralaminar ply is more brittle than VACNTs-resin interlaminar ply. Therefore, VACNTs-resin contact shows high level of bonding comparing to neighbor intralaminar ply in mode I test.

4 | CONCLUSION

The crack propagation behavior in mode I and mode II at reference and nano-reinforced interfaces are investigated in this study. Microscopic and macroscopic results indicate that the behavior of the nano-engineered zone depends on the applied mode.

In mode II, microscopic observations illustrate that the crack path occurs at a VACNTs-resin interface. Moreover, the size and the density of resin cusps observed in the reference ENF samples in the crack path are larger and higher than those observed in the nano-engineered ENF samples. Explained by the presence of VACNTs at the studied interface, these nanotubes occupy most of the interlayer and leave little deformable resin volume for cusps during shearing stress. Thus, the nano-engineered ENF samples exhibit a very brittle behavior and witnesses an unstable crack propagation during the very first compliance loading, whereas the reference ENF sample allows for progressive crack propagation during the third loading.

In mode I, microscopic observations illustrate the crack path within intralaminar interfaces from the beginning of the crack initiation, which is different from mode II observations. The mode I fracture toughness shows little difference between the nano-engineered and reference interfaces ($G_{Ic} \approx 135$ J/m^2). This value is in agreement with the microscopic analysis, which indicates that the crack chooses a more fragile path (intraply in this case) to initiate and propagate.

ACKNOWLEDGMENTS

This work was conducted within the framework of the FUI ATIHS project (Improving satellite structures strength against hypervelocity impacts from space debris) funded by Bpifrance and Région Occitanie. The authors express their gratitude to the partners of the ATIHS project (DynaS+, Thiot Ingenierie, CEA Saclay, CEA Cesta, NAWATechnologies, Armines and Airbus Defense&Space) for the fruitful exchanges carried out in this context. Special thanks are extended to Alexandre Sangar (NAWATechnologies) for helpful discussions and for providing synthetized VACNTs forests on Al-based wafer, to Fabrice Rossi and Williams Brysbaert for sharing experiences in DCB and ENF testing. Finally, the authors would also like to acknowledge to Karine Vieillevigne for her beautiful SEM images.

CONFLICT OF INTEREST STATEMENT

The authors declare no conflict of interest.

DATA AVAILABILITY STATEMENT

The data that support the findings of this study are available from the corresponding author upon reasonable request.

ORCID

Anh Tuan Le https://orcid.org/0000-0003-1596-5465
Quentin Govignon https://orcid.org/0000-0003-0971-0845
Samuel Rivallant https://orcid.org/0000-0002-8882-3161
Thierry Cutard https://orcid.org/0000-0003-1363-9957

REFERENCES

[1] H. Khaledi, Y. Rostamiyan, *Polym. Compos.* **2021**, *42*, 6704.

[2] S. Mamallan, V. Narayanan, *Polym. Compos.* **2022**, *43*, 8170.

[3] G. Rajeshkumar, S. A. Seshadri, S. Ramakrishnan, M. R. Sanjay, S. Siengchin, K. C. Nagaraja, *Polym. Compos.* **2021**, *42*, 3687.

[4] N. Domun, H. Hadavinia, T. Zhang, T. Sainsbury, G. H. Liaghat, S. Vahid, *Nanoscale* **2015**, *7*, 10294.

[5] A. Russo, M. Meo, M. Zarrelli, F. Flora, A. Riccio, *Macromol. Symp.* **2022**, *404*, 2100459.

[6] A. Russo, A. Sellitto, V. Acanfora, M. Zarrelli, A. Riccio, *Macromol. Symp.* **2022**, *404*, 2100458.

[7] Single-shell carbon nanotubes of 1-nm diameter | Nature n.d. https://www.nature.com/articles/363603a0 (accessed: July 2022).

[8] Z. Han, A. Fina, *Prog. Polym. Sci.* **2011**, *36*, 914.

[9] W. Bauhofer, J. Z. Kovacs, *Compos. Sci. Technol.* **2009**, *69*, 1486.

[10] S. Sihn, S. Ganguli, A. K. Roy, L. Qu, L. Dai, *Compos. Sci. Technol.* **2008**, *68*, 658.

[11] H. Huang, C. H. Liu, Y. Wu, S. Fan, *Adv. Mater.* **2005**, *17*, 1652.

[12] T. Borca-Tasciuc, M. Mazumder, Y. Son, S. K. Pal, L. S. Schadler, P. M. Ajayan, *J. Nanosci. Nanotechnol.* **2007**, *7*, 1581.

[13] Y. A. Kim, T. Hayashi, M. Endo, Y. Gotoh, N. Wada, J. Seiyama, *Scr. Mater.* **2006**, *54*, 31.

[14] A. Moisala, Q. Li, I. A. Kinloch, A. H. Windle, *Compos. Sci. Technol.* **2006**, *66*, 1285.

[15] J. K. W. Sandler, J. E. Kirk, I. A. Kinloch, M. S. P. Shaffer, A. H. Windle, *Polymer* **2003**, *44*, 5893.

[16] E. Moaseri, M. Karimi, B. Bazubandi, M. Baniadam, M. Maghrebi, *Polym. Compos.* **2018**, *39*, E1099.

[17] A. Nasirmanesh, A. K. Singh, D. Villaflor, B. Blandford, *Polym. Compos.* **2022**, *43*, 3085.

[18] H. Khosravi, R. Eslami-Farsani, *Polym. Compos.* **2018**, *39*, E677.

[19] K. Bhowmik, N. Khutia, M. Tarfaoui, M. Jana, K. Das, T. Roy, A. Bandyopadhyay, A. Roy Chowdhury, *Polym. Compos.* **2022**, *43*, 7751.

[20] J. Zhu, J. Kim, H. Peng, J. L. Margrave, V. N. Khabashesku, E. V. Barrera, *Nano Lett.* **2003**, *3*, 1107.

[21] J. Zhu, H. Peng, F. Rodriguez-Macias, J. L. Margrave, V. N. Khabashesku, A. M. Imam, K. Lozano, E. V. Barrera, *Adv. Funct. Mater.* **2004**, *14*, 643.

[22] Q.-P. Feng, X.-J. Shen, J.-P. Yang, S.-Y. Fu, Y.-W. Mai, K. Friedrich, *Polymer* **2011**, *52*, 6037.

[23] F. H. Gojny, M. H. G. Wichmann, B. Fiedler, K. Schulte, *Compos. Sci. Technol.* **2005**, *65*, 2300.

[24] R. I. Rubel, M. H. Ali, M. A. Jafor, M. M. Alam, R. I. Rubel, M. H. Ali, *AIMS Mater Sci.* **2019**, *6*, 756.

[25] T. Yokozeki, Y. Iwahori, M. Ishibashi, T. Yanagisawa, K. Imai, M. Arai, T. Takahashi, K. Enomoto, *Compos. Sci. Technol.* **2009**, *69*, 2268.

[26] X.-H. Zhang, Z.-H. Zhang, W.-J. Xu, F.-C. Chen, J.-R. Deng, X. Deng, *J. Appl. Polym. Sci.* **2008**, *110*, 1351.

[27] F. H. Gojny, K. Schulte, *Compos. Sci. Technol.* **2004**, *64*, 2303.

[28] L. Tang, H. Zhang, J. Han, X. Wu, Z. Zhang, *Compos. Sci. Technol.* **2011**, *72*, 7.

[29] L. Sun, G. L. Warren, J. Y. O'Reilly, W. N. Everett, S. M. Lee, D. Davis, D. Lagoudas, H. J. Sue, *Carbon* **2008**, *46*, 320.

[30] G. Gkikas, N.-M. Barkoula, A. S. Paipetis, *Compos. Part B Eng.* **2012**, *43*, 2697.

[31] M. R. Ayatollahi, S. Shadlou, M. M. Shokrieh, *Mater. Des.* **2011**, *32*, 2115.

[32] M. R. Ayatollahi, S. Shadlou, M. M. Shokrieh, *Eng. Fract. Mech.* **2011**, *78*, 2620.

[33] L.-C. Tang, Y.-J. Wan, K. Peng, Y.-B. Pei, L.-B. Wu, L.-M. Chen, L. J. Shu, J. X. Jiang, G. Q. Lai, *Compos. Part Appl. Sci. Manuf.* **2013**, *45*, 95.

[34] T. H. Hsieh, A. J. Kinloch, A. C. Taylor, S. Sprenger, *J. Appl. Polym. Sci.* **2011**, *119*, 2135.

[35] X. F. Yi, A. K. Mishra, N. H. Kim, B.-C. Ku, J. H. Lee, *Compos. Part Appl. Sci. Manuf.* **2013**, *49*, 58.

[36] V. P. Veedu, A. Cao, X. Li, K. Ma, C. Soldano, S. Kar, P. M. Ajayan, M. N. Ghasemi-Nejhad, *Nat. Mater.* **2006**, *5*, 457.

[37] S. S. Wicks, W. Wang, M. R. Williams, B. L. Wardle, *Compos. Sci. Technol.* **2014**, *100*, 128.

[38] A. Salas, C. Medina, J. T. Vial, P. Flores, C. Canales, V. Tuninetti, A. F. Jaramillo, M. F. Meléndrez, *Sci. Rep.* **2021**, *11*, 5000.

[39] E. J. Garcia, B. L. Wardle, H. A. John, *Compos. Part Appl. Sci. Manuf.* **2008**, *39*, 1065.

[40] X. Ni, C. Furtado, N. K. Fritz, R. Kopp, P. P. Camanho, B. L. Wardle, *Compos. Sci. Technol.* **2020**, *190*, 108014.

[41] B. G. Falzon, S. C. Hawkins, C. P. Huynh, R. Radjef, C. Brown, *Compos. Struct.* **2013**, *106*, 65.

[42] Standard Test Method for Determination of the Mode II Interlaminar Fracture Toughness of Unidirectional Fiber-Reinforced Polymer Matrix Composites n.d. https://www.astm.org/d7905_d7905m-19e01.html (accessed: March 2023).

[43] P. Davies, G. D. Sims, B. R. K. Blackman, A. J. Brunner, K. Kageyama, M. Hojo, K. Tanaka, G. Murri, C. Rousseau, B. Gieseke, R. H. Martin, *Plast Rubber Compos.* **1999**, *28*, 432.

[44] Standard Test Method for Mode I Interlaminar Fracture Toughness of Unidirectional Fiber-Reinforced Polymer Matrix Composites n.d. https://www.astm.org/d5528_d5528m-21.html (accessed: March 2023).

[45] A. J. Smiley, R. B. Pipes, *Compos. Sci. Technol.* **1987**, *29*, 1.

Supporting information

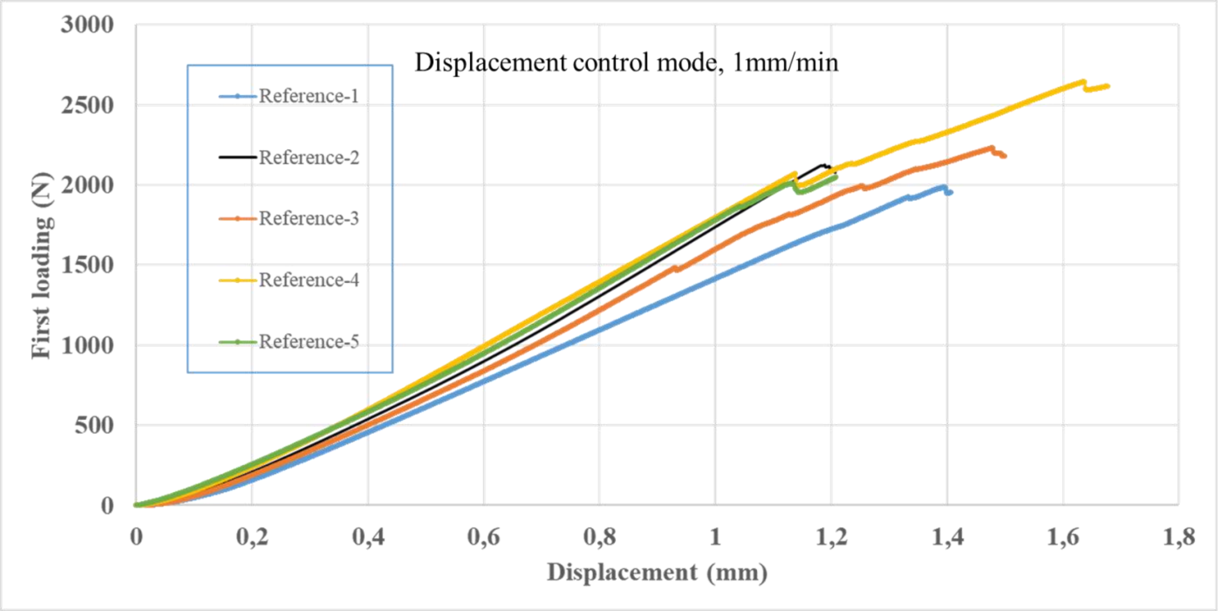

Figure S1 : ENF load-displacement curves of five reference specimens. P_{max} is determined when a drop in the load is observed.

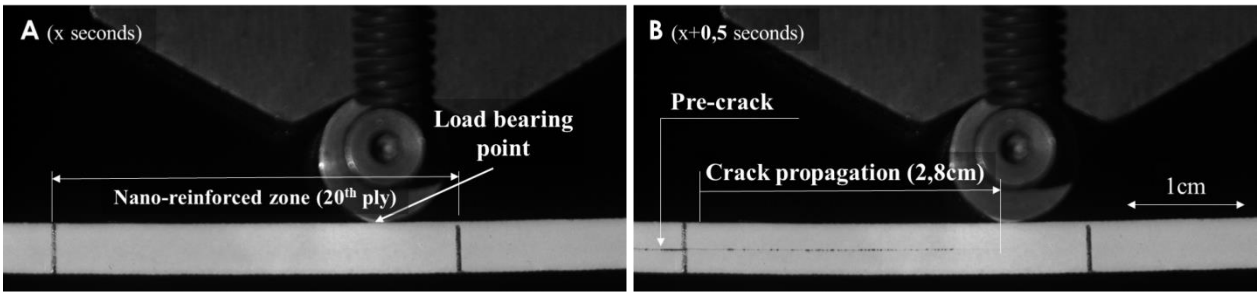

Figure S2 : Images of nano-engineered ENF sample at the end of the first loading: instantaneous and unstable crack propagation from precrack zone to the end of loading point.

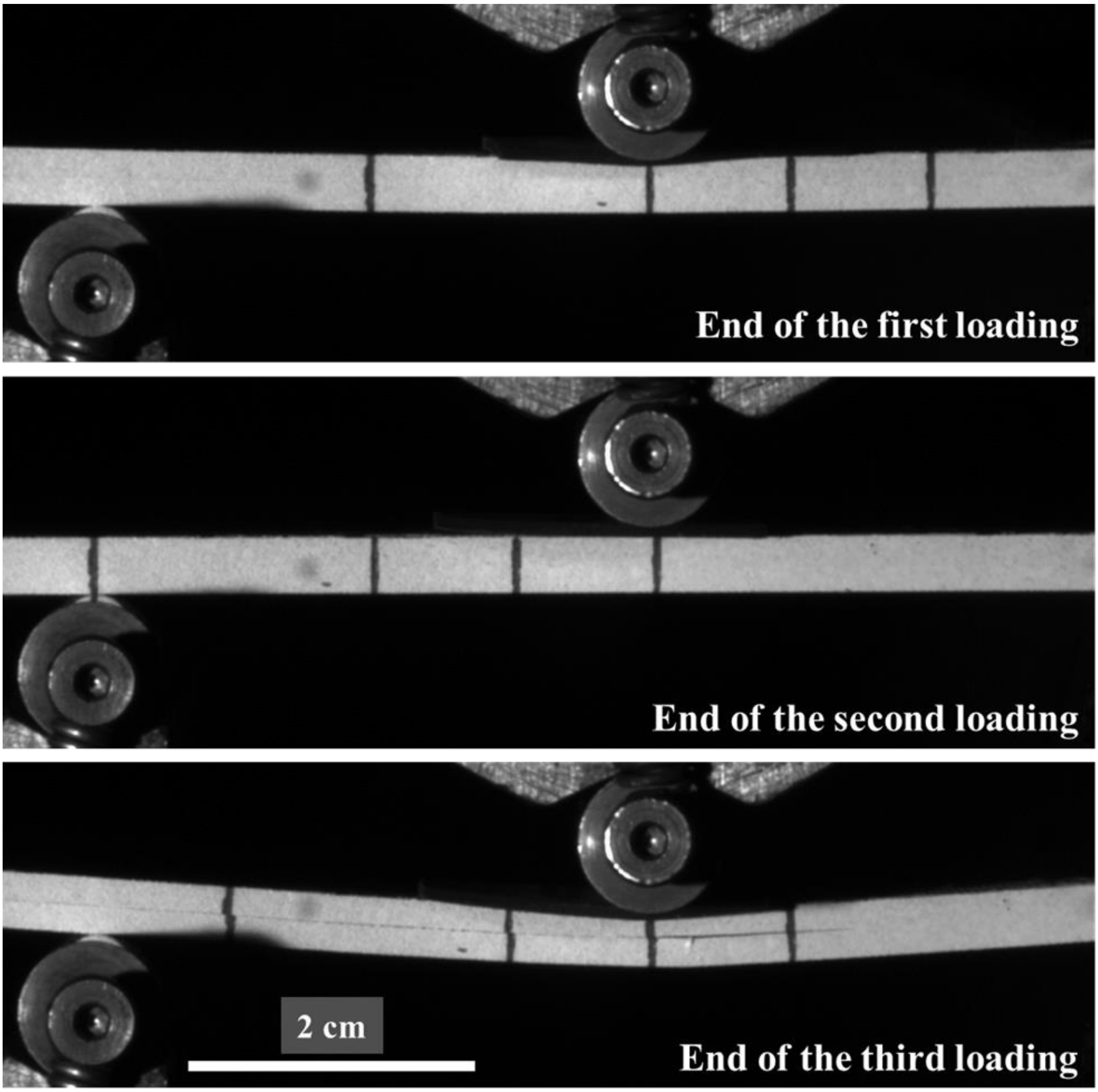

Figure S3 : Images of reference ENF sample : the first two loadings allow to calibrate the sample compliance, crack propagation at the end of the third loading.

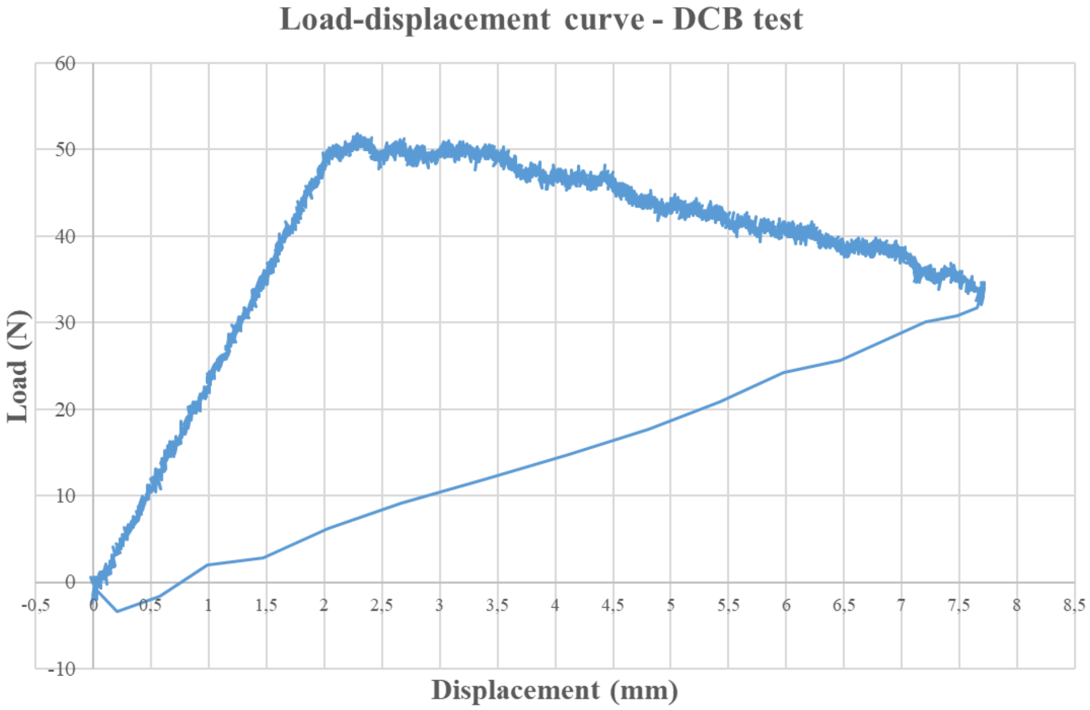

Figure S4 : Load-displacement curve of specimen n°5 during DCB test, similar curves are observed for the other specimens.